SUPPLEMENTAL INFORMATION for

Electrostatic modulation of multiple binding events between loquacious-PD and double-stranded RNA

Sasha A Moonitz[1], Nhat T. Do,[1] Rodrigo Noriega[1,*]

[1] Department of Chemistry, University of Utah, Salt Lake City, UT, USA

* Email: noriega@chem.utah.edu

MATERIALS

INSTRUMENTATION, DATA COLLECTION, and ANALYSIS

MATERIALS

Chemicals. (3-mercaptopropyl)triemethoxysilane (Millipore Sigma, CAS 4420-74-0), (3-glycidyl oxypropyl)triemethoxysilane (Millipore Sigma, CAS 2530-83-8), and TCEP disulfide reducing gel (ThermoFisher cat. #77712) were used as received. Buffers were prepared by diluting sodium acetate (3 M, pH 5.5) in RNase-free water (not DEPC treated) to a concentration of 30 mM.

Protein. Proteins were purchased from ProMab Biotechnologies, Inc. Loquacious, isoform D (Loqs-PD, Uniprot Q9VJY9-4) was expressed from the loqs(e1)-PET21 plasmid in *E. coli.*, purified, and size-verified by SDS-PAGE. Frozen aliquots of Loqs-PD (0.7 mg/mL stock) were dissolved in 30 mM sodium acetate buffer and diluted to a final concentration in the range 0.002 – 38.42 μg/mL

Nucleic Acids. HPLC purified oligonucleotides were purchased from Genscript. For short term storage, the as-received solid precipitates were dissolved in RNase free water with 0.1 mM EDTA to inhibit metal catalyzed nonspecific cleavage of RNA. The resulting solutions had an RNA concentration of 10 μM and were stored at -20 ^{o}C until they were needed for analysis, at which point they were thawed at room temperature immediately prior to measurement. The sequence for 52-nt sense and antisense RNA strands (shown below) is identical to that used in our previous study of dsRNA binding by Dicer-2 and Loqs-PD, with the distinction that the sense strand contains modifications for fluorescence (R_1=C6-Cy3) and for attachment to silane monolayers to functionalize ITO electrodes (for fluorescence R_2=C6-NH_2; for SPR R_2=C6-SH). RNA substrates are purchased as labeled constructs and are annealed after purification by the manufacturer.

Sense (5'→3') **R_1**–GGAGGUAGUAGGUUGUAUAGUAGUAAGACCAGACCCUAGACCAAUUCAUGCC–**R_2**

Antisense (5'→3') GGCAUGAAUUGGUCUAGGGUCUGGUCUUACUACUAUACAACCUACUACCUCC

Doped metal oxide electrodes. ITO sensors for surface plasmon resonance experiments were fabricated as previously described.[1] In brief, sensors are manufactured by sputter deposition of ITO on clean sapphire chips (2.54 cm x 2.54 cm x 0.5 mm, University Wafer) under Ar at room temperature with a DC power of 50 W before annealing under N_2 gas in a rapid thermal annealing oven (Allwin AccuThermo AW610) at 400° C for 2 minutes. Each round of sensor growth included sacrificial glass samples, which reported an average ITO thickness of 189 ± 3 nm measured via stylus profilometry (Tencor P-10) and an average sheet resistance of 11 ± 2. Ω/sq. as determined via 4-point probe measurements (Microtech RF-1). For time-resolved fluorescence experiments, ITO films deposited on unpolished float glass with surface resistivities of 8-12 Ω/sq. and L x W x D dimensions of 25 mm x 25 mm x 1.1 mm were purchased from Millipore Sigma. Chips were cleaned via sequential sonication baths in a detergent solution (Alconox), acetone, isopropyl alcohol, and HPLC grade water for 15 minutes in each solution before drying with filtered N_2. Clean ITO chips were then immersed for 1 hr in a 1:1:5 v/v% solution of 30% (w/w) hydrogen peroxide, ammonia, and HPLC grade water, followed by RNase decontamination (RNaseZap™, ThermoFisher) before drying in an 80° C oven for 30 min. After functionalization and measurement, substrates are not reused to prevent any carryover of signal from previous functionalization rounds.

INSTRUMENTATION, DATA COLLECTION, and ANALYSIS

Molecular dynamics simulations of Loqs-PD structure. Currently available structures for loqs-PD or its complexes have a limited coverage of the loqs-PD sequence. For example, in cryo-EM structures of complexes of loqs-PD with Dicer-2 and dsRNA (PDB: 7W0A-F; 8HF0-1),[2,3] the majority of the structure corresponds to Dicer-2 and the dsRNA substrate – only the 16 C-terminal residues of loqs-PD are resolved. High-quality models for loqs-PD are limited to standalone

structures of its dsRBMs determined by NMR (PDB: 5NPG, 5NPA).[4] However, the relative position and orientation of loquacious-PD's tandem dsRBMs, as well as the conformation of the remaining ~200 aa residues, remain unknown. Seeking a more complete description of the loquacious-PD structure that includes its linker and terminal domains, we employ computational models. As a starting point, we employ the structure of loquacious-PD predicted by the trRosetta server (**Fig. S1a**).[5] The intrinsically disordered structure of large part of this protein is evident, as only 202 out of 359 amino acid residues have a Local Distance Difference Test[6] (lDDT) score at or above 0.6, and these better-described regions are mainly located in the dsRBM domains (**Fig. S1a**). This initial structure was parameterized in Amber23[7] using the *ff14SBonlysc* force field,[8] *mbondi3* intrinsic radii set, and the generalized Born neck 2 implicit solvent model.[9] Two rounds of energy minimization (2500 steps of steepest descent constraining the positions of all heavy atoms in the protein backbone, then 2500 steps of conjugate gradient with constrained C_α atomic positions) preceded an annealing step from 60 K to 300 K in 0.6 ns, which was followed by an unconstrained 200 ns long equilibration run at 300 K using a Langevin thermostat with 2 ps^{-1} collision frequency. Simulation steps were 2 fs and frames were recorded every 10 ps. A Debye-Huckel screening parameter of electrostatic interactions was set to correspond to a 150 mM concentration of mobile monovalent salt ions in solution. The root-mean-square (rms) displacement (**Fig. S1b**) of the model indicates it has reached a sufficiently equilibrated structure (**Fig. S1c**). A PDB file format of the equilibrated structure (Fig. 1, Fig. S1.c) is provided as supplementary information with this manuscript.

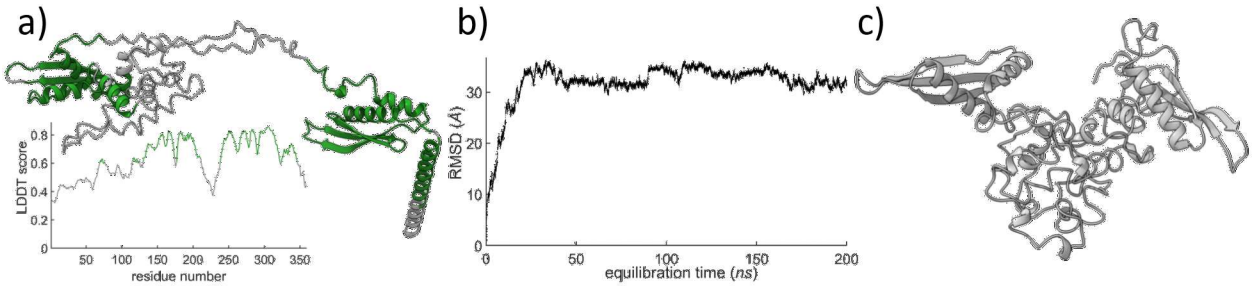

Figure S1. Model for the structure of the full loquacious-PD protein. (a) The trRosetta server was used to predict the structure of Loqs-PD (Uniprot Q9VJY9-4), and its local Distance Difference Test score as an indicator of the accuracy in the predicted structure; protein regions with lDDT ≥ 0.6 highlighted in green. **(b)** The rms displacement for the model as a function of simulation time shows its approach to an equilibrated structure **(c)**.

SPR sample preparation and data collection. ITO-sapphire sensor chips were affixed to a triangular SF11 right-angle coupling prism (15 mm side) using high refractive index optical epoxy (Norland NOA170) on the sapphire face. A sensor chip and a blank sapphire window separated by a Teflon spacer (1 mm thickness, 25 mm inner diameter) were mounted on a custom-built open-top liquid cell, which provides access to the sample compartment for the addition of liquid samples and the insertion of counter and reference electrodes. Contact to the ITO working electrode was made outside the liquid compartment. Following assembly, SPR sensors were loaded on a rotation stage where pulsed *p*-polarized mid-infrared light (2550 nm output of Coherent TOPAS-Prime, pumped by Coherent Astrella) was focused into the prism. The lasing and measurement setup have been previously described.[1]

Spatial heterogeneity in the ITO film (e.g., thickness, roughness, density of mobile charges) as well as in the attachment of dsRNA targets can affect the detected SPR response. However, these effects are accounted for in our experiments by conducting extensive *in situ* characterization of each sensor – recording their reflectivity *vs*. incidence angle prior to binding experiments, as well as quantifying sensor response at high protein concentrations. Besides these onboard calibrations,

ex situ measurements of thickness and conductivity were performed and provide further information on sensor characteristics. Prior to RNA functionalization and protein addition, SPR curves recorded in air and with 30 mM sodium acetate buffer (**Figure S2**) were used to characterize the ITO sensors and determine the sensing angle ($\theta_{sens.}$) for binding measurements. The measured reflectivity was ~87% of the predicted value (which already accounts for reflective losses at the air/prism interface); this reduced intensity is comparable to the expected absorptive loss due to the long (~1.5 cm) optical path in the SF11 coupling prism (β_{loss}~75%).[10]

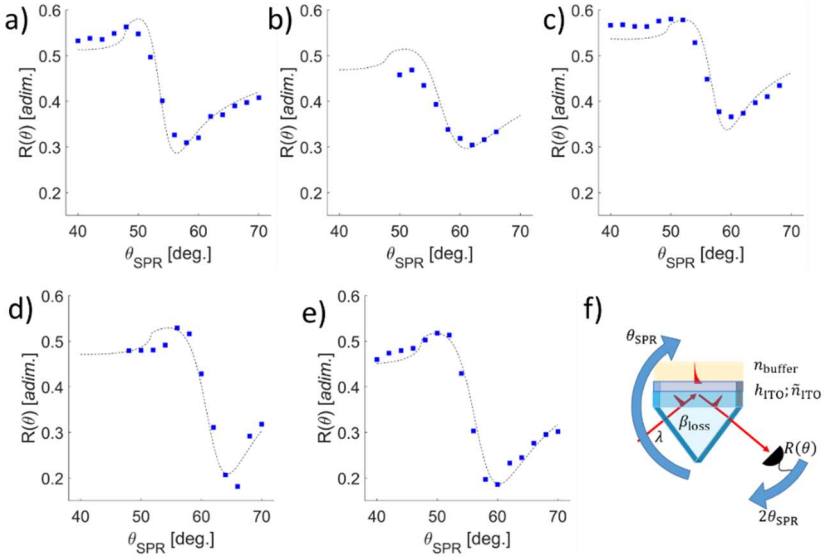

Figure S2. Characterizing the plasmonic resonance of sensor chips. The mid-IR SPR response is shown as the reflectance *vs.* incidence angle; collected data as blue squares, transfer matrix fits (WinSpall™) as dashed lines. Each panel **(a-e)** corresponds to a different sensor used to collect a protein:RNA binding isotherm; binding measurements for **(a, d)** are in Figure 1 while those for **(b, c, e)** are in Figure S3 (listed in order of appearance). A sketch of the experimental configuration and parameters used in the fitting of SPR curves is also shown **(f)**.

Table S1. SPR sensor parameters obtained by fitting their plasmon resonance responses.

	Individual samples					**mean ± std. dev**
	open circuit			with external bias		
N_e ($\times 10^{20}$cm^{-3})	5.5	3.8	4.9	4.3	3.6	**4.6 ± 0.7**
h_{ITO} (nm)	210	262	244	227	236	**235 ± 16**
$\partial R/\partial n$ (adim.)	7.5	4.8	4.6	8.2	7.4	**6.3 ± 1.4**

Conjugation of thiol-modified dsRNA with mercaptosilane[11] was carried out by first reducing disulfide bridges present in both nucleotide and silane solutions. Two separate microcentrifuge tubes were loaded with 200 µL of TCEP reduction slurry, centrifuged for 1 min at 1000 x g, and the supernatant was discarded. The precipitate was washed 5 times with 30 mM NaOAc buffer (for each wash: resuspend, centrifuge, discard supernatant). Stock solutions of RNA (10 µM in RNase free water with 0.1 mM EDTA) and silane (2.69 mM in 30 mM NaOAc buffer) were loaded to the washed gel and allowed to incubate for 45 min at room temperature. Once disulfide reduction was complete, the silane and RNA solutions were mixed in a 1:5 RNA:silane molar ratio and the conjugation reaction was allowed to proceed for 1 hr at room temperature. This solution of mercaptosilane—thiol-dsRNA conjugates was then added to the SPR sample cell with a clean and activated ITO surface (set to the sensing angle, θ_s) and incubated for 15 min to achieve *in situ* surface functionalization. After functionalization, residual RNA/silane was washed out with fresh buffer, and a fresh solution of 200 µL of buffer was loaded prior to protein binding experiments (as a protein-free starting point). To apply an electric bias, the sample cell was connected to a potentiostat (CH Instruments 700E) – the current response was entirely non-faradaic. Loqs-PD was then introduced to the sample chamber by sequential addition of aliquots of protein stock solutions, and the reflectivity is monitored for a period of 5 min. after each addition.

It is possible that silane functionalization affects the roughness and/or conductivity near the sensor's surface, but such potential differences are minor and do not affect the overall sensor's SPR response as evidenced by comparison of SPR curves collected for the same sensor prior to and immediately following functionalization (**Fig. S3**). The position and sharpness of SPR resonances are largely unaffected. To mitigate the uncertainty in reflectance due to variability in angle position during SPR curve collection, the functionalization process was monitored with

measurements at constant incidence angle (**Fig. S3**, inset). The only effect observed is a shift in the baseline SPR reflectivity of pristine *vs.* silanized ITO resulting from the change in dielectric constant of the molecular layer at the ITO surface (alkyl layer *vs.* buffer).

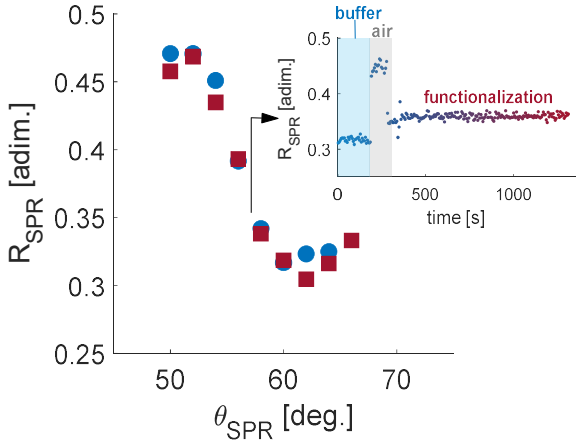

Figure S3. SPR response is stable to functionalization. Surface plasmon resonance curves for the same sensor before and after functionalization are shown in blue and red, respectively. (inset) A time trace of reflectivity vs. time at constant sensing angle was collected during functionalization, showing changes in signal when buffer was taken out of the sample cell and refilled with the functionalization solution.

Fitting the binding response of mid-IR SPR chips. As mentioned in the main text, the evanescent wave of mid-IR plasmon resonances extends deeper into the sample than typical penetration depths for visible wavelength noble metal plasmonics.[12] Due to the exponential decay of this evanescent wave, SPR resonances are most sensitive to dielectric changes in close proximity to the conductor/dielectric interface – which is why they display a response to protein binding surface-anchored targets. Due to this binding, the reflectivity is expected to follow a Langmuir isotherm response, $R(c_{loqs}) = R_0 + A \cdot c_{loqs}/(c_{loqs} + K_D)$ where the reflectivity starts from a value R_0 in the absence of protein and saturates to a value $R_0 + A$ when the concentration of protein c_{loqs} is much larger than the dissociation constant K_D. However, the larger penetration depth of mid-IR

plasmons extends beyond the layer where molecular recognition takes place, and at high enough protein concentrations it responds to refractive index changes in the bulk solution. Assuming the refractive index change is proportional to protein concentration and remains in the small-response SPR region (e.g., no switch to off-resonance conditions), this bulk response can be approximated as $R(c_{loqs}) = R_0 + \left[\frac{\partial R}{\partial c} \cdot (c_{loqs} - c^*)\right] \cdot H(c_{loqs} - c^*)$ where c^* is the protein concentration at which a given sensor's plasmon resonance is affected by bulk conditions, which we include as a Heaviside step function $H(c_{loqs} - c^*)$. Including these two components of the SPR signal (binding and bulk), it is possible to extract not only the dissociation constant for Loqs-PD:dsRNA complexes observed in each set of conditions, but also estimate the surface coverage at saturation $\Gamma_{prot} \approx (A \cdot \delta_{SPR}) \cdot \left({}^{\partial R}/_{\partial c}\right)^{-1}$ and, together with the chip's sensitivity (**Table S1**), the change in refractive index with protein concentration ${}^{\partial n}/_{\partial c} \approx {}^{\partial R}/_{\partial c} \cdot \left({}^{\partial R}/_{\partial n}\right)^{-1}$.

Table S2. SPR response parameters for measurements of Loqs-PD:dsRNA complex formation atop ITO electrodes. Uncertainties for individual trials report the confidence interval from fitting routines, or the propagated uncertainty (for Γ_{prot}). Uncertainties for mean values report the standard error of the mean.

	Open circuit ($N = 3$)				**+500 mV vs. Ag/AgCl** ($N = 2$)		
	individual trials			**mean**	**individual trials**		**mean**
K_D (nM)	177 ± 87	68 ± 41	124 ± 116	**120 ± 50**	231 ± 172	325 ± 186	**280 ± 130**
A (adim.)	5.8 ± 1.5	3.3 ± 0.3	4.5 ± 1.7	**4.5 ± 0.8**	6.2 ± 2.6	9.0 ± 3.3	**7.6 ± 2.1**
${}^{\partial R}/_{\partial c}$ ($\times 10^3 \mathrm{M}^{-1}$)	19.1 ± 1.9	9.4 ± 1.1	10.7 ± 0.2	**13.1 ± 0.7**	28.4 ± 4.3	22.3 ± 5.3	**25.4 ± 3.4**
Γ_{prot}($\times 10^{10}$ cm^{-2})	2.5 ± 0.9	1.8 ± 0.5	2.1 ± 0.3	**2.2 ± 0.4**	1.3 ± 0.6	2.4 ± 1.1	**1.9 ± 0.6**
c^* (nM)	284 ± 36	650 ± 390	410 ±110	**450 ± 140**	295 ± 37	300 ± 55	**297 ± 33**

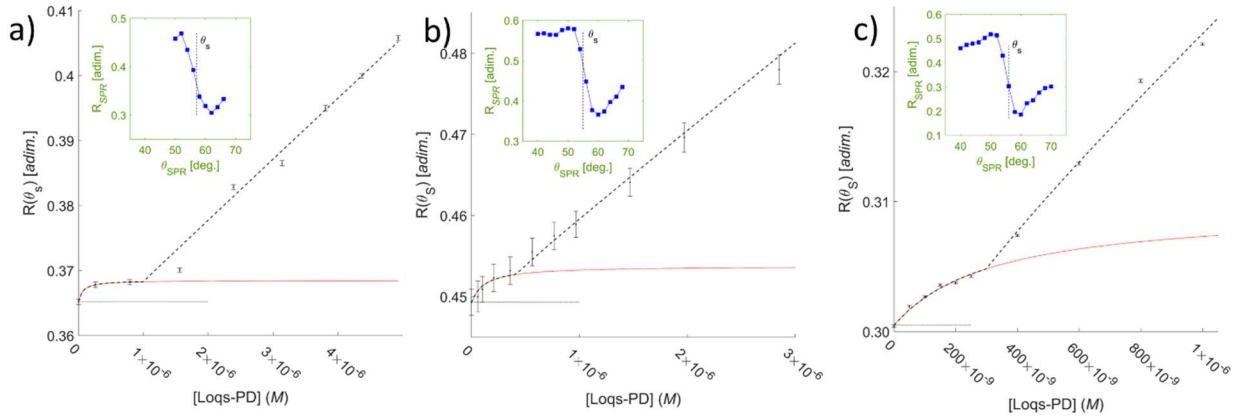

Figure S4. Mid-infrared plasmons response to protein recognition of surface-tethered dsRNA targets. As in Fig. 2 in the main text, the reflectance of a mid-IR ($\lambda = 2550$ nm) laser beam coupled to the surface plasmon resonance of ITO electrodes increases as protein is added to the sample chamber. Experiments were carried out under open circuit conditions **(a,b)** and with an applied voltage of 500 mV vs. Ag/AgCl **(c)**. Markers indicate measured reflectance, averaged over 5 mins.; error bars are ± one standard error of the mean. A horizontal line indicates the reflectance starting value R_0. A binding isotherm (red line) is combined with a linear response to describe the observed signal (combined fit as dashed black lines). Insets depict the measured plasmon resonance for each sensor in blank buffer (blue squares), with the sensing angle θ_s marked by a vertical dotted line.

Batch-to-batch variability in sensor deposition affects the sharpness and sensitivity of the plasmon resonance (**Fig. S2**, **Table S1**) and its response to protein addition (**Figs. 2** and **S4**, **Table S2**); and non-idealities in sensor/detector positioning preclude variable-angle measurements when reflectance values with a 10^{-3} resolution are required. Therefore, wide-angle scans with multiple dielectric media followed by fixed-angle scans during binding are optimal, which in turn requires *in situ* functionalization while monitoring a pre-selected location on the sample. Thus, inhomogeneities in target attachment led to differences in surface coverage $\Gamma_{prot} = 1.3 - 2.5 \times 10^{10}$ cm^{-2}. Measurements are robust to this variability, except when surface functionalization (at the spot chosen for alignment and monitoring) is too low to result in a detectable signal. In such rare cases, the sensor response lacks a clear binding signal and displays only a bulk response (**Fig. S5**).

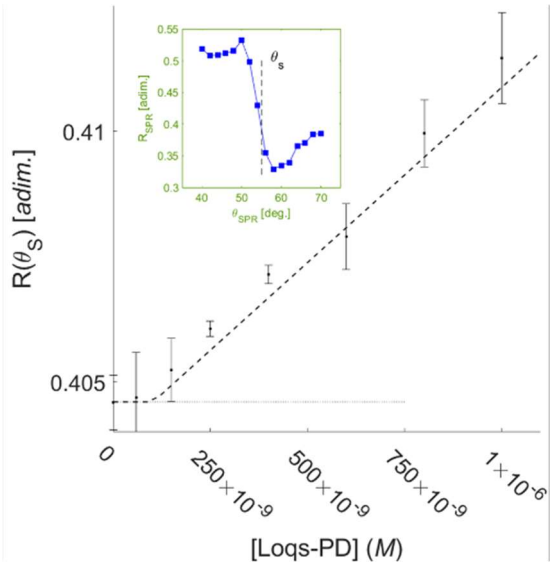

Figure S5. Bulk response in mid-IR SPR. Inhomogeneous surface coverage and variable chip sensitivity can result in a lack of a measurable binding response, with the change in reflectance due entirely to changes in bulk solution refractive index. As in Fig. 2, markers indicate measured reflectance, averaged over 5 mins.; error bars are ± one standard error of the mean. A horizontal line indicates the reflectance starting value R_0. A linear response describes the observed signal (dashed black line), with a slope $^{\partial R}/_{\partial c} = 7 \times 10^3 \mathrm{M}^{-1}$ and a turn-on concentration $c^* = 100$ nM. Inset: measured plasmon resonance in blank buffer, with the sensing angle θ_s marked by a vertical dotted line.

Efficiency of surface functionalization. To compare the surface coverage of Loqs-PD estimated with mid-IR SPR experiments to the surface density of dsRNA binding targets, we determined the efficiency of dsRNA attachment to ITO SPR sensors. Using X-ray photoelectron spectroscopy (XPS; Kratos Axis Ultra), we measured the elemental composition of 3 separate regions of functionalized ITO electrodes. To rule out degradation, freshly-prepared and aged (1 week) samples were compared. Survey scans (**Fig. S6**) indicate the presence of In and Sn (from ITO support), Si (from silane self-assembled monolayer), P (from RNA), as well as C and O (several sources, including possible contamination). High resolution scans were collected to quantify the elemental composition of the samples, with atomic percentages (ϕ_x) reported in **Table S3**.

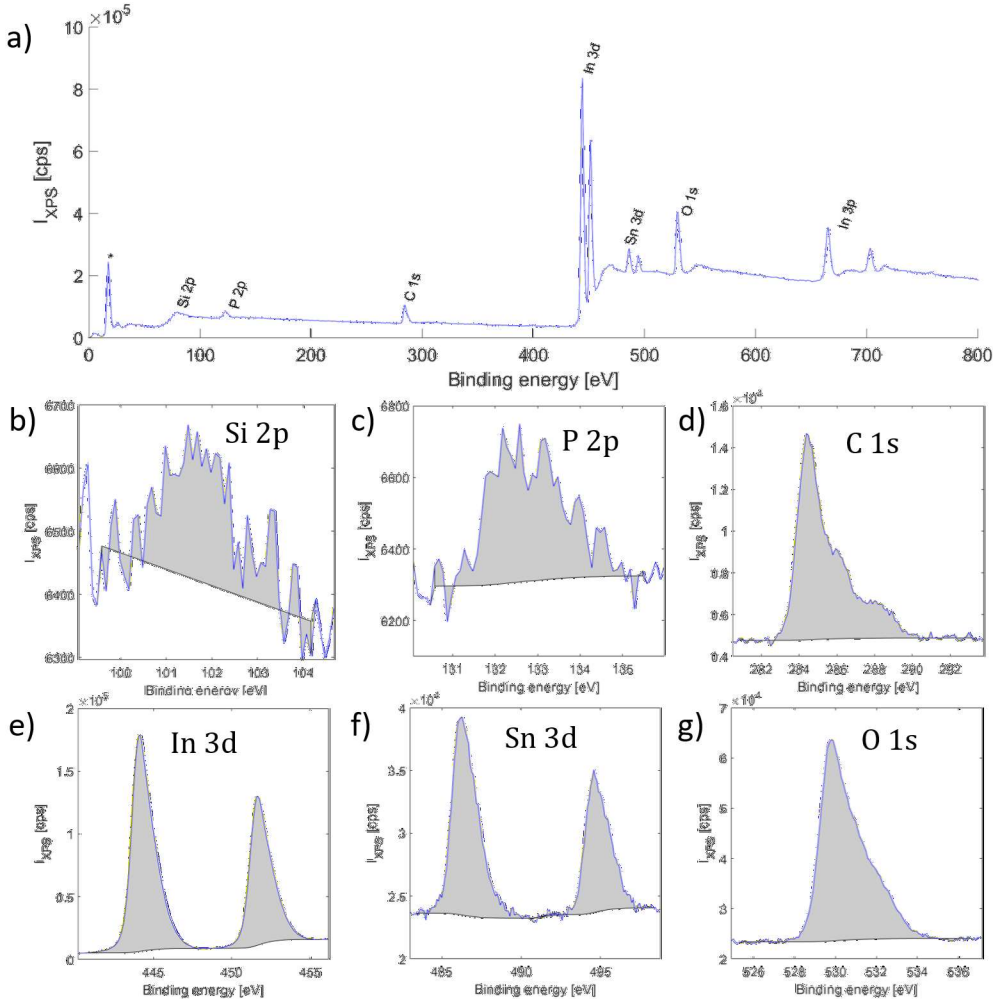

Figure S6. Composition analysis of functionalized ITO electrodes. (a) XPS survey scan identifies the sample components, with each photoelectron peak labeled. Lowest energy peak (*) is unassigned, as it can arise from several sources (e.g., In 4d, Sn 4d, C 2s, O 2s). **(b-g)** High-resolution scans show collected signal (blue lines), background (black lines), and integrated area (gray) used to quantify relative abundance of each element. Measurement area is approximately 300 μm by 700 μm, with collection depth of ~10 nm.

The amount of phosphorous (ϕ_{P}) normalized by the number of P atoms per dsRNA ($n_{\mathrm{P}} = 104$) was divided by the amount of silicon (ϕ_{Si}; number of Si atoms per silane $n_{\mathrm{Si}} = 1$) to yield a mean functionalization efficiency $\langle \eta_{fxn} \rangle \approx 1\%$; i.e., ~1% of the silanes have a dsRNA attached. The coverage of silane molecules on the ITO electrode was estimated as the ratio of silicon to indium, $\langle {\phi_{\mathrm{Si}}}/{\phi_{\mathrm{In}}} \rangle \approx 2\%$, multiplied by the density of In atoms on an ITO surface ($\Gamma_{\mathrm{In}} \sim 10^{14}$ cm^{-2}).[13]

The surface coverage of dsRNA was thus estimated to be $\Gamma_{RNA} \sim 10^{10}$ cm^{-2}. While XPS signals (particularly Si and P) are not strong enough to yield a highly accurate quantification typical for semiconductor or surface catalysis studies, the values extracted from these experiments provide a valuable order of magnitude estimate and serve as comparison for our main findings from mid-IR experiments – which we find are in agreement. The surface density of silanes (10^{12} cm^{-2}) is comparable to standard surface functionalization protocols and reflects a high-quality SAM (i.e., effective silane-ITO coupling). The amount of nucleic acids at the surface is ~100X lower than the number of silane groups, and its density is deliberately sparse to avoid crowding effects – at $\sim 10^{10}$ cm^{-2}, the average distance between binding sites is 100 nm; about 10X larger than the size of a complex.

Table S3. Elemental composition (in atomic %) measured with XPS for functionalized ITO electrodes. To account for heterogeneity, three separate regions of each sensor were probed (one near the center and two near the edges). To rule out sample degradation, a freshly-prepared sample is compared to an aged one.

Sample		Si	P	C	In	Sn	O
fresh	spot 1	0.5	0.7	29.7	24.1	2.2	42.9
	spot 2	0.5	0.7	30.4	24.0	2.2	42.2
	spot 3	0.5	0.5	30.2	24.1	2.2	42.5
aged (~1 week)	spot 1	0.3	0.5	30.5	24.5	2.2	41.9
	spot 2	0.5	0.7	31.2	24.3	2.2	41.1
	spot 3	0.4	0.6	30.5	24.4	2.2	41.8

Sample preparation, data collection, and analysis for time-resolved fluorescence experiments. Surface functionalization for time-resolved fluorescence measurements begins by cleaning chips as described in the mid-IR SPR section above, then submerging the clean ITO chips to a bath of 1% (3-glycidyl oxypropyl)triemethoxysilane in ethanol for 20 mins. Sensors were then rinsed in ethanol and cured for 1 hr in a 110° C oven. Once the silane curing process was complete, Cy3-dsRNA with an amine linker was attached to the self-assembled monolayer epoxide groups. A

solution of functionalized dsRNA in 0.1 M KOH was dotted on the ITO sensor and allowed to react for 36 hr. in decontaminated Petri dishes, followed by rinsing with RNase-free water to ensure that only attached nucleotides contribute to the fluorescence signal.[14–16] Silane-oxide coupling is fast and efficient, but the epoxy-amine and disulfide bridging reactions for RNA covalent attachment are less efficient and slower. Moreover, the choice of a functionalization protocol preceding or following sample assembly reflects the need to perform characterization of the sensor properties (for SPR) and the requirement to avoid free-floating probe in the sample chamber (most relevant for fluorescence). For fluorescence, any remaining dye-dsRNA targets in the sample chamber would be detected as background emission and their binding by protein in solution would confound the signal from surface-anchored probes. Therefore, ex situ functionalization and substantial post-attachment rinsing is necessary. Conversely, sequential attachment of silane to the ITO and RNA to the silane is needed because the long incubation time (36 hrs for epoxy-amine coupling) would lead to the formation of long silane chains and lead to poor SAM formation – silane polymerization is limited when the silane-oxide coupling is performed separately, or for the much shorter incubation times for disulfide bridging.

Samples were then loaded onto the previously described liquid cell, electrodes were attached/inserted, and the cell assembly was positioned at the focal spot of a previously-described polarization-resolved ultrafast fluorescence instrument.[1,17] Before buffer addition, fluorescence signal was optimized by adjusting the position of the excitation beam on the sample with an XY micrometer stage. Data was collected in time-tagged time-resolved mode, which keeps track of three tags for each detected photon: the delay between photon arrival and the previous excitation pulse (microtime) to measure the excited state lifetime, the time elapsed since data collection began (macrotime) to measure time-dependent changes in photophysics, and the detection channel

(vertical or horizontal polarization) to compute rotationally-averaged intensity as well as transient fluorescence anisotropy. Data processing was performed as described previously for thin fluorescent peptide films. Poisson counting statistics were assumed for photon detection, and uncertainty was propagated through the analyses described below.

Time-averaged photophysical observables were obtained by grouping all photons within the widest possible macrotime window – if equilibration was observed, data was limited to post-equilibration; in the absence of time-dependent changes, the entire dataset was used. For each fluorescence trace, the mean fluorescence lifetime τ_{FL} was computed by a weighted average of photon arrival times. Transient anisotropy decays often contained substantial noise, which precluded accurate fitting of rotational diffusion times. However, residual fluorescence anisotropy on ~ns time scales contains information on the slow tumbling dynamics of large biomolecules and is a more robust observable. This residual anisotropy r_∞ was computed by averaging within a time window after the time-dependent fluorescence anisotropy had decayed to a flat baseline. Changes in photophysical observables (τ_{FL} or r_∞) as a result of concentration-dependent protein binding were described by nonlinear least-squares fitting to standard Langmuir isotherms – e.g., $\tau_{FL}(c_{loqs}) = \tau_0 + \Delta\tau \cdot c_{loqs}/(c_{loqs} + K_D)$.

Kinetic measurements were computed by grouping all photons by their macrotime arrival (ten 48 s windows), using their channel and microtime information to construct the fluorescence and transient anisotropy decays within each window (optimized to achieve good signal while also providing temporal information). Within each window, data was analyzed in the same way as for time-averaged observations. Kinetic traces of mean fluorescence lifetime vs. macrotime (**Fig. S7**) were fit to an exponential relaxation $\tau_{FL}(t) = \tau_\infty - \Delta\tau \cdot \mathrm{e}^{-k_{eq} \cdot t}$ and equilibration rates were used to compute association and dissociation rates (**Table S4**).

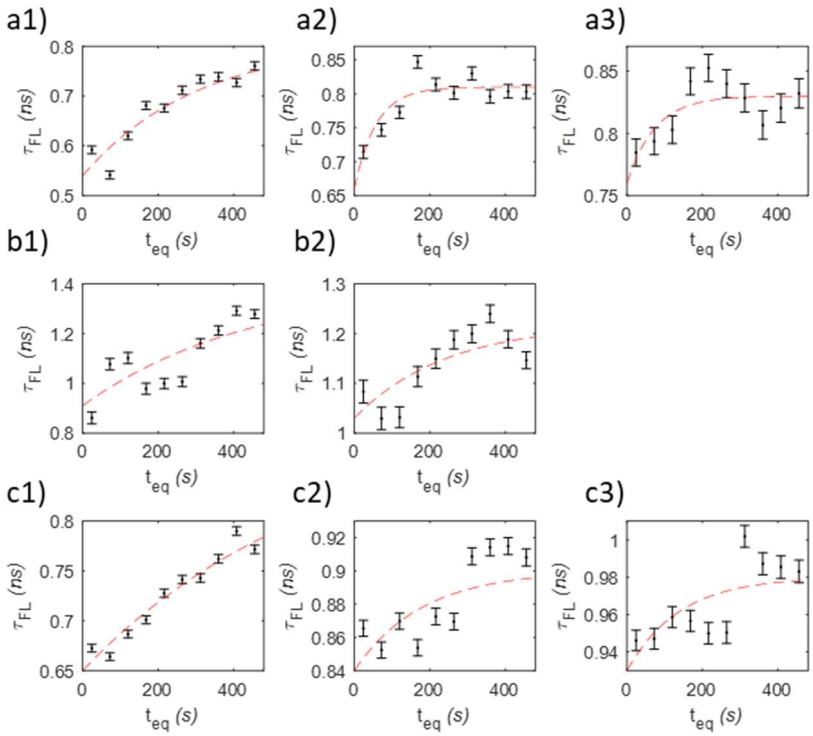

Figure S7. Kinetic measurements of mean fluorescence lifetime. The equilibration dynamics of mean fluorescence lifetime can be used to extract the rate at which binding equilibrium is achieved as a function of protein concentration. Panels **(a1-3)** contain data for the low concentration regime highlighted in Fig. 3c ($[\text{loqs} - \text{PD}] = 0.26, 0.51, 0.77$ pM), while panels **(b1-2)** contain data for the high protein concentration regime in the same sample ($[\text{loqs} - \text{PD}] = 0.5$,1 μM in Fig. 3c). Panels **(c1-3)** correspond to the sub-pM region highlighted in Fig. 3b ($[\text{loqs} - \text{PD}] = 0.08, 0.2, 0.37$ pM). Data represented as black markers with errorbars to display their standard deviation, exponential relaxation fits shown as red dotted lines.

Table S4. Binding parameters obtained from kinetics measurements of mean fluorescence lifetime, whose equilibration time scales are dictated by association and dissociation rates of Loqs-PD:dsRNA complexes ($k_{eq} = k_{on} \cdot c_{Loqs} + k_{off}$). The equilibrium dissociation constants predicted by these microscopic rates ($K_D = k_{off}/k_{on}$) are also shown.

High-affinity binding (a1-3 & c1-3 in Fig. S6)	
$\boldsymbol{k_{on}}$ $(\times \mathbf{10^{10}M^{-1}s^{-1}})$	2.1
$\boldsymbol{k_{off}}$ $(\times \mathbf{10^{-4}s^{-1}})$	4.6
$\boldsymbol{K_D}$ $(\times \mathbf{10^{-13}M})$	0.2

Low-affinity binding (b1-2 in Fig. S6)	
$\boldsymbol{k_{on}}$ $(\times \mathbf{10^{3}M^{-1}s^{-1}})$	3.8
$\boldsymbol{k_{off}}$ $(\times \mathbf{10^{-4}s^{-1}})$	3.0
$\boldsymbol{K_D}$ $(\times \mathbf{10^{-9}M})$	80

AUTHOR CONTRIBUTIONS

SAM constructed the experimental apparatus, carried out measurements, and performed an initial round of data analysis, interpretation, and manuscript preparation. NTD assisted with measurements and sample preparation, performed all computational work, and contributed to manuscript preparation. RN designed the project, guided its development, and finalized the analysis and manuscript preparation.

REFERENCES

[1] S. A. Moonitz, N. Shepard, R. Noriega, *J. Mater. Chem. B* 2020, *8*, 7024.

[2] T. Deng, S. Su, X. Yuan, J. He, Y. Huang, J. Ma, J. Wang, *Nature Communications* 2023, *14*, 5228.

[3] S. Su, J. Wang, T. Deng, X. Yuan, J. He, N. Liu, X. Li, Y. Huang, H.-W. Wang, J. Ma, *Nature* 2022, *607*, 399.

[4] J.-N. Tants, S. Fesser, T. Kern, R. Stehle, A. Geerlof, C. Wunderlich, M. Juen, C. Hartlmüller, R. Böttcher, S. Kunzelmann, O. Lange, C. Kreutz, K. Förstemann, M. Sattler, *Nucleic Acids Res* 2017, *45*, 12536.

[5] Z. Du, H. Su, W. Wang, L. Ye, H. Wei, Z. Peng, I. Anishchenko, D. Baker, J. Yang, *Nat Protoc* 2021, *16*, 5634.

[6] V. Mariani, M. Biasini, A. Barbato, T. Schwede, *Bioinformatics* 2013, *29*, 2722.

[7] [a] D. A. Case, H. M. Aktulga, K. Belfon, D. S. Cerutti, G. A. Cisneros, V. W. D. Cruzeiro, N. Forouzesh, T. J. Giese, A. W. Götz, H. Gohlke, S. Izadi, K. Kasavajhala, M. C. Kaymak, E. King, T. Kurtzman, T.-S. Lee, P. Li, J. Liu, T. Luchko, R. Luo, M. Manathunga, M. R. Machado, H. M. Nguyen, K. A. O'Hearn, A. V. Onufriev, F. Pan, S. Pantano, R. Qi, A. Rahnamoun, A. Risheh, S. Schott-Verdugo, A. Shajan, J. Swails, J. Wang, H. Wei, X. Wu, Y. Wu, S. Zhang, S. Zhao, Q. Zhu, T. E. I. Cheatham, D. R. Roe, A. Roitberg, C. Simmerling, D. M. York, M. C. Nagan, K. M. Jr. Merz, *J. Chem. Inf. Model.* 2023, *63*, 6183
[b] D.A. Case, H.M. Aktulga, K. Belfon, I.Y. Ben-Shalom, J.T. Berryman, S.R. Brozell, D.S. Cerutti, T.E. Cheatham, III, G.A. Cisneros, V.W.D. Cruzeiro, T.A. Darden, N. Forouzesh, G. Giambaşu, T. Giese, M.K. Gilson, H. Gohlke, A.W. Goetz, J. Harris, S. Izadi, S.A. Izmailov, K. Kasavajhala, M.C. Kaymak, E. King, A. Kovalenko, T. Kurtzman, T.S. Lee, P. Li, C. Lin, J. Liu, T. Luchko, R. Luo, M. Machado, V. Man, M. Manathunga, K.M. Merz, Y. Miao, O. Mikhailovskii, G. Monard, H. Nguyen, K.A. O'Hearn, A. Onufriev, F. Pan, S. Pantano, R. Qi, A. Rahnamoun, D.R. Roe, A. Roitberg, C. Sagui, S. Schott-Verdugo, A. Shajan, J. Shen, C.L. Simmerling, N.R. Skrynnikov, J. Smith, J. Swails, R.C. Walker, J. Wang, J. Wang, H. Wei, X. Wu, Y. Wu, Y. Xiong, Y. Xue, D.M. York, S. Zhao, Q. Zhu, and P.A. Kollman (2023), *Amber 2023*, University of California, San Francisco.

[8] J. A. Maier, C. Martinez, K. Kasavajhala, L. Wickstrom, K. E. Hauser, C. Simmerling, *J. Chem. Theory Comput.* 2015, *11*, 3696.

[9] H. Nguyen, D. R. Roe, C. Simmerling, *J. Chem. Theory Comput.* 2013, *9*, 2020.

[10] SCHOTT Optical parameters datasheet https://www.us.schott.com/shop/medias/SCHOTT-datasheet-SF11.pdf (Last accessed 2023-12-20).

[11] A. Kumar, O. Larsson, D. Parodi, Z. Liang, *Nucleic Acids Research* 2000, *28*, e71.

[12] J. Dostálek, C. J. Huang, W. Knoll, in *Surface Design: Applications in Bioscience and Nanotechnology*, n.d.

[13] V. M. Bermudez, A. D. Berry, H. Kim, A. Piqué, *Langmuir* 2006, *22*, 11113.

[14] R. Pruna, F. Palacio, M. Martínez, O. Blázquez, S. Hernández, B. Garrido, M. López, *Interface Focus* 2016, *6*, DOI 10.1098/rsfs.2016.0056.

[15] D.-W. Zhang, N. Papaioannou, N. M. David, H. Luo, H. Gao, L. C. Tanase, T. Degousée, P. Samorì, A. Sapelkin, O. Fenwick, M.-M. Titirici, S. Krause, *Mater. Horiz.* 2018, *5*, 423.

[16] J. B. Lamture, K. L. Beattie, B. E. Burke, M. D. Eggers, D. J. Ehrlich, R. Fowler, M. A. Hollis, B. B. Kosicki, R. K. Reich, S. R. Smith, *Nucleic Acids Res* 1994, *22*, 2121.
[17] S. A. Moonitz, R. Noriega, *Macromolecular Rapid Communications* 2023, *44*, 2200635.